Renewable Energy 64 (2014) 132–143

Contents lists available at ScienceDirect

Renewable Energy

journal homepage: www.elsevier.com/locate/renene

Numerical simulation of a submerged cylindrical wave energy converter

M. Anbarsooz*, M. Passandideh-Fard, M. Moghiman

Department of Mechanical Engineering, Ferdowsi University of Mashhad, Mashhad 9177948944, Iran

ARTICLE INFO

Article history:
Received 19 April 2013
Accepted 1 November 2013
Available online

Keywords:
Wave energy converter
Wave-body interactions
Submerged cylinder
Bristol cylinder

ABSTRACT

In this study, a numerical model based on the complete solution of the Navier–Stokes equations is proposed to predict the behavior of the submerged circular cylinder wave energy converter (WEC) subjected to highly nonlinear incident waves. The solution is obtained using a control volume approach in conjunction with the fast-fictitious-domain-method for treating the solid objects. To validate the model, the numerical results are compared with the available analytical and experimental data in various scenarios where good agreements are observed. First, the free vibrations of a solid object in different non-dimensional damping ratios and the free decay of a heaving circular cylinder on the free surface of a still water are simulated. Next, the wave energy absorption efficiency of a circular cylinder WEC calculated from the model is compared with that of the available experiments in similar conditions. The results show that tuning the converter based on the linear theory is not satisfactory when subjected to steep incident waves while the numerical wave tank (NWT) developed in the current study can be effectively employed in order to tune the converter in such conditions. The current NWT is able to predict the wave-body interactions as long as the turbulence phenomena are not important which covers a wide range of Reynolds and Keulegan-Carpenter numbers.

1. Introduction

The wave energy as a renewable energy has inspired numerous inventors and motivated many experimental and numerical investigations. Yet, several reviews have been published in this regard two of which are the book of McCormik [1] and a recent review paper by Falcao [2]. Although various types of wave energy converters (WECs) have been designed, no single technology has yet been recognized to be superior to the others.

The design of several WECs is based on the oscillatory motion of a submerged or floating part against a fixed reference. Depending on the water depth, different types of WECs might be more efficient in terms of energy absorption. The vertical force component of the waves are the main source of energy in the offshore WECs such as the floating buoys while near-shore devices, like bottom-hinged flaps, utilize the horizontal force component. A device where both the horizontal and vertical force components can be absorbed was first proposed by Evans [3]; this device includes a horizontally aligned cylinder that can move elliptically during the wave. He derived a linear theory for the performance of this class of wave energy absorbing bodies. The submerged cylinder exhibits a large efficiency (up to 100% theoretically) in a wide range of wave frequencies [3]. Dean [4] and Ogilvie, [5] using linear wave diffraction theory, showed that no energy is reflected from the cylinder whether it is fixed or freely buoyant. This fact is also valid for a case where the cylinder is constrained by springs and dampers in two orthogonal directions and the constants of spring and damper are the same in both directions [3]. Evans showed that for certain constants of the spring and damper corresponding to a given frequency, the transmitted wave would also be eliminated resulting in the complete absorption of the incident wave energy. Very recently, Heikkinen et al. [6] using the potential flow theory, investigated the effect of phase shift, cylinder radius, wave height and wave period on the efficiency of the submerged cylinder wave energy converter.

For wave energy applications, a good agreement has been reported experimentally in several studies (see for example [7]) between the results of the linear theory and those of the experiments in small ($H/L < 0.01$) to moderate wave steepness ($0.01 < H/L < 0.03$), where H and L being the wave height and length, respectively. However, for steep waves ($H/L > 0.03$) or in the wave conditions that excite resonances, due to non-linear and/or viscous effects, considerable discrepancies have been reported in the literature. Evans et al. [8] and Davis [9] demonstrated that the linear theory completely fails to predict the performance of the

* Corresponding author. Tel.: +98 511 8763304; fax: +98 511 8626541.
E-mail address: m.anbarsooz@gmail.com (M. Anbarsooz).

0960-1481/$ – see front matter © 2013 Elsevier Ltd. All rights reserved.
http://dx.doi.org/10.1016/j.renene.2013.11.008

submerged cylindrical wave energy absorbers for steep waves. This drawback of the linear theory is mainly due to its limiting assumptions namely assuming the flow to be linear and irrotational, and neglecting the viscosity effects.

A common practice to consider the effects of viscosity is to add a damping term similar to the drag term in the well-known Morison's equation [10]. This method has been employed by Davis [9] and Babarit et al. [11]. In this method, however, estimating the drag coefficient is a major problem. Although there are many experimental results available in the literature to determine the drag coefficient, this methodology leads to a poor prediction of the absorption efficiency [9] and considerable uncertainties in the results [11]. Therefore, considering a constant value for the drag coefficient for an elliptically moving cylinder will lead to unrealistic wave forces.

In this study, the behavior of a submerged cylinder WEC is simulated using the complete solution of the Navier–Stokes equations in conjunction with the fast fictitious domain method [12] for treating the solid objects. The numerical model is a modified version of the one previously developed by Mirzaii and Passandideh-Fard [13] for modeling fluid flows containing a free surface in presence of an arbitrary moving object. Using this numerical model, the wave forces on the submerged cylinder containing the viscous drag forces are calculated via solving the Navier–Stokes equations in each time step. The results of the proposed model show a good agreement with those of the experiments even for steep waves.

2. Mathematical model

2.1. Problem setup

The schematic of the computational domain shown in Fig. 1 is a rectangular numerical wave tank ($Lc \times Hc$) equipped with a flap-type wavemaker and two passive damping zones. A solid object representing the flap-type wavemaker is positioned at $x = Xp$ from the left, and the circular cylinder representing the wave absorber is initially placed at $x = Ls$ in the submergence depth S_d measured from the free surface. The cylinder is moored to the bottom of the tank via springs and dampers aligned at 45 degrees with respect to the x-axis.

The solid object representing the flap-type wavemaker is forced to move according to a prescribed harmonic motion in order to generate a desired wave. The domains of computations based on Fig. 1 are considered as: $Lc > 8L$, $Hc > 1.5d$, $Ld1 = 0.25$ m and $Ld2 > 2L$. More details on the wave generation methodology used in this study is given elsewhere [14]. The generated waves travel toward the submerged cylinder and force it to move; as a result, some parts of the wave energy are absorbed by the dampers.

2.2. Fluid flow

The governing equations for fluid flow are the Navier–Stokes equations in two-dimensional, Newtonian, incompressible and laminar flow:

$$\nabla \cdot \vec{V} = 0 \tag{1}$$

$$\frac{\partial \vec{V}}{\partial t} + \vec{V} \cdot \nabla \vec{V} = -\frac{1}{\rho}\nabla p + \frac{1}{\rho}\nabla \cdot \vec{\tau} + \vec{g} + \frac{1}{\rho}\vec{F}_b \tag{2}$$

$$\vec{\tau} = \mu\left[(\nabla \vec{V}) + (\nabla \vec{V})^T\right] \tag{3}$$

where $\vec{V}$ is the velocity vector, ρ the density, μ the dynamic viscosity, p the pressure, $\vec{\tau}$ the stress tensor and $\vec{F}_b$ represents body forces acting on the fluid. The interface is advected using Volume-of-Fluid (VOF) method by means of a scalar field (F), the so-called liquid volume fraction, defined as:

$$F = \begin{cases} 0 & \text{in the gas phase} \\ 0 <, \ < 1 & \text{in the liquid} - \text{gas interface} \\ 1 & \text{in the liquid phase} \end{cases} \tag{4}$$

The discontinuity in F is a Lagrangian invariant, propagating according to:

$$\frac{dF}{dt} = \frac{\partial F}{\partial t} + \vec{V} \cdot \nabla F = 0 \tag{5}$$

2.3. Solid object treatment

As seen in Fig. 1, the solid objects that move within the computational domain are the flap-type wavemaker and the submerged circular cylinder which acts as the wave energy absorber. Both objects are modeled via the fast-fictitious-domain method [13] where the fluid flow equations are enforced everywhere in the computational domain including fluid and solid zones. This conceptual framework leads to a simple geometry and time independent computational domain which can be discretized by a structured and fixed grid mesh resulting in a considerable reduction of the required time for computations. There are several numerical approaches presented based on the fast-fictitious domain method such as those of Glowinski et al. [15,16], Patankar [17], Patankar et al. [18] and Sharma and Patankar [12]. The numerical method used in this study is a modified version of the Sharma and Patankar model [12] developed by Mirzaei and Passandideh-Fard

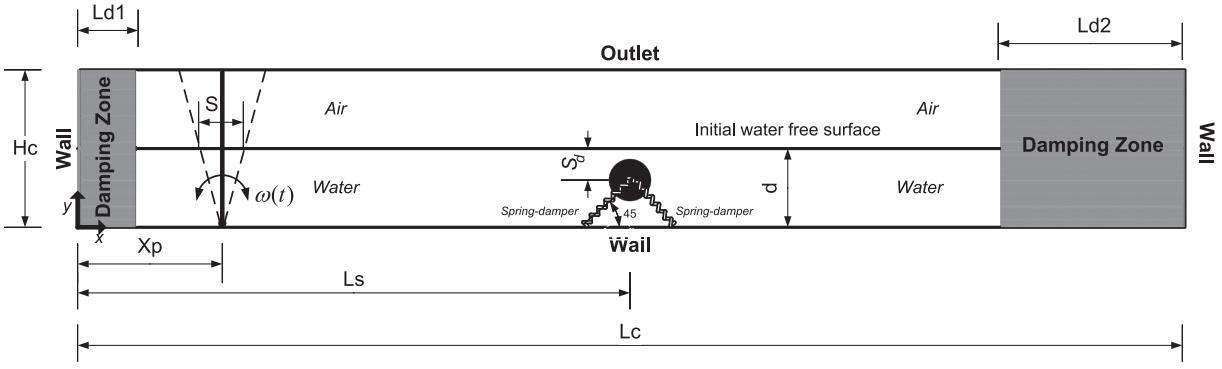

Fig. 1. Schematic of the computational domain.

[13]. This method is capable of handling unprescribed motion of the solids without solving any additional equation in the computational domain. The no-slip condition on the solid–liquid interface is imposed by attributing a high viscosity to the solid objects. In the first stage of a computation in each time step, the governing equations of fluid motion are solved everywhere in the computational domain including the solid zone without any additional equation. Next, the rigid body motion for the submerged cylinder can be obtained by imposing an additional condition that the total linear and angular momentums in the solid body must be conserved in each time step. For the flap-type wavemaker, however, the flap angular velocity is determined based on a harmonic motion calculated to generate a desired wave [14]. Then, a velocity change based on the average values is imposed only within the solid zones; the change, however, is not projected into the fluid domain. Considering an average velocity for the solid, leads to an unrealistic slip condition in the solid–liquid interface as stated by Sharma and Patankar [12]. Therefore, in this study, a high viscosity is attributed to the solid zone [13]. A summary of the computational procedure followed in each time step of simulation is given below:

1) The solid object in the computational domain is identified using a scalar parameter φ_s defined as:

$$\varphi_s = \begin{cases} 0 & \text{Out of the solid} \\ 0 <, \ < 1 & \text{Solid boundary} \\ 1 & \text{Within the solid} \end{cases} \tag{6}$$

2) The fluid flow equations are solved everywhere in the computational domain including the solid zone. In this step, the density and viscosity in each cell are defined as:

$$\rho = F\rho_l + (1 - F - \varphi_s)\rho_g + \varphi_s\rho_s \tag{7}$$

$$\mu = F\mu_l + (1 - F - \varphi_s)\mu_g + \varphi_s\mu_s \tag{8}$$

where subscripts l, g and s refer to liquid, gas and solid, respectively. The viscosity of the solid is set by a large magnitude in comparison with that of the liquid. This large magnitude of viscosity implicitly imposes the no-slip condition on the solid–liquid interface. It has been shown elsewhere [13] that using a viscosity two orders of magnitude larger than that of the fluid is large enough to have an accurate solid body movement. It should be noted that within the solid zone, the value of F is set to zero.

3) The average translational and rotational velocities in the solid zones are obtained. For the solid object representing the flap-type wavemaker, these velocities are calculated based on the flap prescribed harmonic motion; while for the solid zone representing the submerged cylinder they are obtained based on the conservation of the momentum in the solid using following integrals:

$$M_s\vec{V}_s = \int_{\text{Solid zone}} \rho\vec{V}\,\mathrm{d}\forall \tag{9}$$

$$I_s\vec{\omega}_s = \int_{\text{Solid zone}} \vec{r}\times\rho\vec{V}\,\mathrm{d}\forall \tag{10}$$

The velocity distribution inside the solid zone is then updated accordingly. When the velocity in the computational domain is updated, the interface is advected using Eq. (5).

2.4. Spring and damper forces

The effects of the external forces, which are the spring and damper forces in this study, on the rigid body motion of the cylinder are considered by imposing an additional body force in the momentum equation for the computational cells inside the solid zone. At each time step, this body force per unit mass of the solid object is determined based on the spring and damper forces of the previous time step according to the following relation:

$$\vec{a}_{\text{added}} = \frac{\sum \vec{F}_{\text{external}}}{M_s} \tag{11}$$

The above equation is applied in the two orthogonal directions as:

$$a_{x,\text{added}} = \frac{\sum F_{x,\text{external}}}{M_s} = \frac{-k_{sx}\left(x_{c,s} - x_{\text{free}}\right) - c_x U_s}{M_s} \tag{12}$$

$$a_{y,\text{added}} = \frac{\sum F_{y,\text{external}}}{M_s} = \frac{-k_{sy}\left(y_{c,s} - y_{\text{free}}\right) - c_y V_s}{M_s} \tag{13}$$

where k_{sx}, k_{sy}, c_x, c_y are the spring constants and damping coefficients in the x and y directions, respectively. U_s, V_s and M_s are the horizontal velocity, vertical velocity and the mass of the solid object. $x_{c,s}$, $y_{c,s}$ are the center positions of the solid cylinder and x_{free}, y_{free} are the spring free lengths in the x and y directions, respectively.

2.5. Absorption efficiency

The wave energy absorbed by the cylinder in one wave period may be calculated as:

$$E_{\text{abs}} = \int_t^{t+T} P_{\text{abs}}(t)\mathrm{d}t = \int_t^{t+T} \vec{F}_{\text{wave}}(t)\cdot\vec{V}_s(t)\mathrm{d}t \tag{14}$$

where $P_{\text{abs}}(t)$ is the instantaneous absorbed power, $\vec{F}_{\text{wave}}(t)$ the wave excitation force acting on the cylinder, and $\vec{V}_s(t)$ represents the cylinder velocity. The total force, $\vec{F}_{\text{tot}}(t)$, consists of the spring, damper, buoyancy and the wave excitation forces. According to the Newton's second law:

$$\begin{aligned} \vec{F}_{\text{tot}}(t) &= \vec{F}_{\text{spring}}(t) + \vec{F}_{\text{damper}}(t) + \vec{F}_{\text{bouyancy}}(t) + \vec{F}_{\text{wave}}(t) \\ &= M_s\frac{\mathrm{d}\vec{V}_s(t)}{\mathrm{d}t} \end{aligned} \tag{15}$$

Hence the wave excitation force can be written as:

$$\vec{F}_{\text{wave}}(t) = M_s\frac{\mathrm{d}\vec{V}_s(t)}{\mathrm{d}t} - \vec{F}_{\text{spring}}(t) - \vec{F}_{\text{damper}}(t) - \vec{F}_{\text{bouyancy}}(t) \tag{16}$$

The energy absorption efficiency is the ratio of the mean absorbed power, $\overline{P}_{\text{abs}}$, to the total mean wave power, $\overline{P}_w$, calculated as [6]:

$$\eta = \frac{\overline{P}_{abs}}{\overline{P}_{w}} = \frac{\frac{1}{T}\left[\int_{t}^{t+T} P_{abs}(t)\mathrm{d}t\right]}{\frac{1}{8}\rho_{w} g H^2 c_g} \tag{17}$$

where T is the wave period, ρ_w the water density, g the gravitational acceleration, H the wave height and c_g is the wave group velocity. Because of the periodic motion of the cylinder, neither the spring forces nor the buoyancy and inertia forces have an effect on the mean absorber power; i.e.:

$$\frac{1}{T}\left[\int_{t}^{t+T} \vec{F}_{spring}(t)\cdot\vec{V}_s(t)\mathrm{d}t\right] = 0 \tag{18}$$

$$\frac{1}{T}\left[\int_{t}^{t+T} \vec{F}_{bouyancy}(t)\cdot\vec{V}_s(t)\mathrm{d}t\right] = 0 \tag{19}$$

$$\frac{1}{T}\left[\int_{t}^{t+T} M_s\frac{\mathrm{d}\vec{V}_s(t)}{\mathrm{d}t}\cdot\vec{V}_s(t)\mathrm{d}t\right] = 0 \tag{20}$$

Thus, the absorption efficiency can be calculated using the following:

$$\eta = \frac{\frac{1}{T}\left[\int_{t}^{t+T} -\vec{F}_{damper}(t)\cdot\vec{V}_s\mathrm{d}t\right]}{\frac{1}{8}\rho g H^2 c_g} \tag{21}$$

Since $\vec{F}_{damper}(t) = -c\vec{V}_s(t)$, therefore:

$$\eta = \frac{\frac{1}{T}\left[\int_{t}^{t+T} c\vec{V}_s\cdot\vec{V}_s\mathrm{d}t\right]}{\frac{1}{8}\rho g H^2 c_g} = \frac{\frac{1}{T}\left[\int_{t}^{t+T} c_x u_s^2\mathrm{d}t + \int_{t}^{t+T} c_y v_s^2\mathrm{d}t\right]}{\left(\frac{1}{8}\rho g H^2\right)\frac{1}{2}\cdot\frac{L}{T}\left[1+\frac{2kd}{\sinh 2kd}\right]} \tag{22}$$

where L is the wave length, k the wave number and d is the still water level.

3. Numerical method

For the discretization of the governing equations, a three-step projection method is used in which the continuity and momentum equations are solved in three fractional steps [13]. In the first step, the convective and body force terms in the momentum equations are discretized using an explicit scheme. The viscosity and pressure terms in this step are not considered. An intermediate velocity field, $V^{n+1/3}$, is then obtained as:

$$\frac{\vec{V}^{n+1/3}-\vec{V}^{n}}{\delta t} = \left(-\vec{V}\cdot\nabla\vec{V}\right)^n + \frac{1}{\rho^n}\vec{F}_b^n \tag{23}$$

In this study, the no-slip condition on the solid–liquid interface is imposed by attributing a high viscosity to the solid region. As a result, the allowable time step for numerical simulation will decrease dramatically if the viscous term discretization is performed using an explicit scheme. This fact is due to a linear stability time step constraint for an explicit scheme [19]. Therefore, in the second step, an implicit discretization scheme is used to model the viscous term of the momentum equation to obtain the intermediate velocity from this step, $V^{n+2/3}$, as:

$$\frac{\vec{V}^{n+2/3}-\vec{V}^{n+1/3}}{\delta t} = \frac{1}{\rho^n}\nabla\cdot\mu\left[\left(\nabla\vec{V}^{n+2/3}\right)+\left(\nabla\vec{V}^{n+2/3}\right)^T\right] \tag{24}$$

In this equation, the viscous term is discretized in the fractional time step $t^{n+2/3}$. This leads to an implicit treatment of the viscous term which, in turn, allows using a large time step for simulation of fluids with high viscosities. Eq. (24) is solved using a TDMA (Tri-Diagonal Matrix Algorithm) method to obtain $V^{n+2/3}$.

In the final step, the second intermediate velocity is projected to a divergence free velocity field as:

$$\frac{\vec{V}^{n+1}-\vec{V}^{n+2/3}}{\delta t} = -\frac{1}{\rho^n}\nabla p^{n+1} \tag{25}$$

The continuity equation is also satisfied for the velocity field at the new time step:

$$\nabla\cdot\vec{V}^{n+1} = 0 \tag{26}$$

Taking the divergence of Eq. (25) and substituting from Eq. (26) results in a pressure Poisson equation as:

$$\nabla\cdot\left[\frac{1}{\rho^n}\nabla p^{n+1}\right] = \frac{\nabla\cdot\vec{V}^{n+2/3}}{\delta t} \tag{27}$$

The obtained pressure field can then be used to find the final velocity field by applying Eq. (25). The resulting set of equations is symmetric and positive definite; a solution is obtained in each time step using an Incomplete Cholesky–Conjugate Gradient (LDLT) solver [20]. Eq. (5) is used to track the location of the interface and is solved according to the Youngs PLIC algorithm [21]. More details regarding the model and the free surface treatment are given elsewhere [13].

The initial condition considered in this study is a still water with no velocity and no surface waves. The solid cylinder is at its equilibrium position at rest. At the left, right and bottom boundaries of the computational domain, as displayed in Fig. 1, the no slip condition for the velocity components is imposed. At the top of the domain, the outlet boundary with atmospheric pressure is used. Two passive absorption zones, one just behind the wavemaker and the other at the end of the computational domain are considered in the simulations. The method used for treating these damping regions is increased viscosity to a level high enough to effectively damp the energy of the incident waves [14].

4. Results and discussion

Certain aspects of the proposed model have been previously validated in other studies [13,14]. They include the ability of the model to simulate the interaction of a solid object with a liquid in presence of a free surface [13] and the wave generation method [14]. In this study, therefore, the new developments in the model will be examined. For this purpose, first, an analytical case (free vibrations of a solid object) is considered where the accuracy of the methodology used to apply the external forces to the solid object is tested. Next, the problem of the free decay of a heaving circular cylinder is studied and the results are compared with the available analytical and experimental data. Finally, the wave energy absorption efficiency at various wave frequencies is compared with the experimental results of Davis [9].

4.1. Free vibrations of a solid object

The first case considered for simulation is a single-degree-of-freedom system with a viscous damper as shown in Fig. 2. If the system, after an initial disturbance, is left to vibrate on its own, the free vibration will continue until all the energy is dissipated by the damper. The available analytical solutions for such an oscillating system are classified based on the value of the damping ratio, $\varsigma = c/c_{cr}$, where c is the damping coefficient, $c_{cr} = 2\sqrt{k_s M_s}$ the critical damping coefficient, k_s the spring constant and M_s is the mass of the solid object [22]. Depending on the damping ratio, ς, the system is called under-damped for $\varsigma < 1$, critically damped for $\varsigma = 1$ and over-damped for $\varsigma > 1$. The computational domain considered for this simulation is a rectangle (0.5 m × 2.0 m) given in Fig. 3.

A solid circular cylinder with a diameter of 0.2 m is initially placed at ($x = 0.25$ m, $y = 1.6$ m). The figure shows the contour of φ_s which defines the solid zone according to Eq. (6). The cylinder is connected to the ground ($y = 0$) by a spring which has a free length of 1.3 m and a spring constant of 500 N/m. The solid cylinder is surrounded by atmospheric air with reduced viscosity to eliminate the viscous drag forces on the solid sphere. From a mesh refinement study, it was found that for a mesh size corresponding to 10 cells per cylinder radius (CPR), the results were mesh-independent. Also a time step equal to $T/100$ (where T is the oscillation period of the un-damped system) is found to be sufficiently small such that the results were independent of the time step. Fig. 4 shows the center positions of the solid cylinder as a function of time for different values of the damping ratio: $\varsigma = 0.1$ and 0.5 for under-damped systems, $\varsigma = 1.0$ for a critically-damped system, and $\varsigma = 1.5$ for an over-damped system. The figure shows a good agreement between the numerical results and those of the analytics for all values of the damping ratio. The velocity vectors at an intermediate time, $t/T = 0.77$, for the critically-damped system are shown in Fig. 5. Two recirculation zones formed behind the falling cylinder can be well observed in this figure. The close comparison between the simulations and analytics is an indication of the accuracy of the model for the external forces.

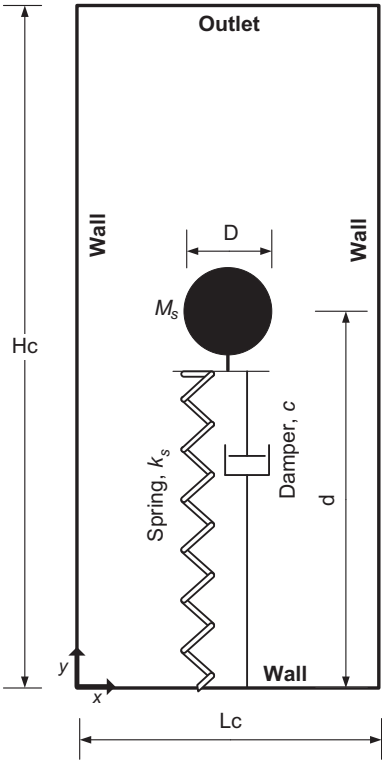

Fig. 2. Schematic of an oscillating system with a single degree of freedom.

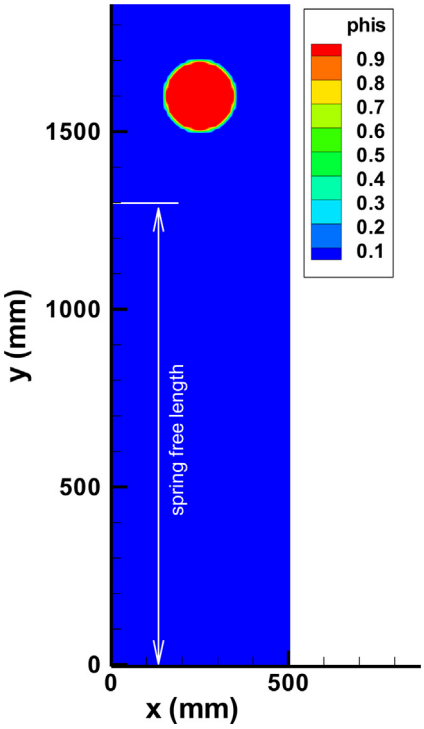

Fig. 3. Contour of solid volume fraction φ_s at $t = 0.0$ s for the free vibration of a circular solid cylinder (Fig. 2).

4.2. Free decay of a heaving circular cylinder

Consider a solid circular cylinder floating on the free surface of an infinitely deep liquid. If the cylinder is slightly disturbed from its stable equilibrium position in the direction normal to the free surface, it will oscillate in a heave motion until the cylinder and the liquid return to their equilibrium state at rest. An analytical solution for such a transient motion of a half-submerged circular cylinder in heaving oscillations is available in the literature [23,24]. Ito [25]

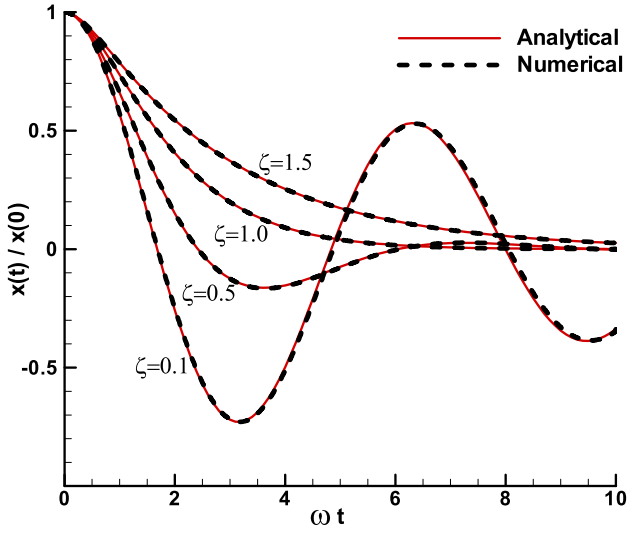

Fig. 4. Center positions of the solid cylinder of Fig. 2 as a function of time for different values of the damping ratio.

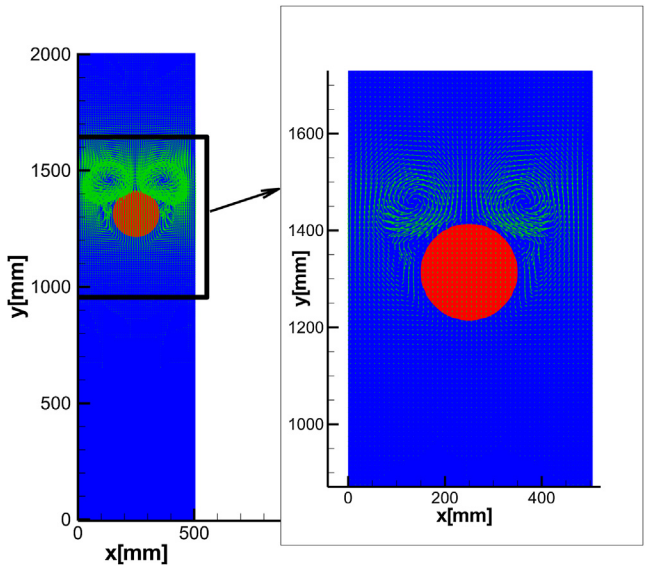

Fig. 5. Velocity vectors at $t/T = 0.77$ for the critically damped vibrations ($\varsigma = 1.0$) of the solid cylinder of Fig. 2.

also studied the problem experimentally where a good agreement between the experimental results and those of the analytics was obtained. This case with similar conditions, as shown in Fig. 6, has been investigated in this study to better illustrate the capabilities of the proposed model. A solid circular cylinder with a radius of 0.1 m in a water depth of 1.6 m ($d/R = 16$) is given an initial disturbance of 0.03 m ($y_0/R = 0.3$) and is left to oscillate on the water free surface. The dimensions of the computational domain and the boundary conditions are shown in Fig. 6. The right boundary is selected 4.0 m away from the center of the cylinder; a high viscosity damping zone is also considered at this boundary to avoid any free surface wave reflections during the simulation. The density of the solid cylinder is half of the water, $\rho_s = 500\ \mathrm{kg/m^3}$.

The center position of the cylinder as a function of the non-dimensional time, $t\sqrt{g/R}$, in comparison with the experimental results of Ito [25] and those of the analytics [24] is shown in Fig. 7. As observed, the cylinder motion in y-direction approximately follows a harmonic oscillatory motion in time with damping amplitude [19]. The results of simulations are given for four different mesh sizes characterized by the number of cells per cylinder radius (CPR). As seen from the figure, a mesh size corresponding to 20CPR guaranteed grid independent results. The simulated results agree well with those of the experiments and analytics; this validates the model and its underlying assumptions.

4.3. Submerged cylinder wave energy converter

In this section, the numerical model is applied to a more realistic application involving the behavior of a submerged circular cylinder WEC, the so-called "Bristol cylinder". The cases considered are similar to those performed by Davis in his experiments [9]. A circular cylinder with a diameter of $D = 0.1$ m, a water depth $d = 0.35$ m, and a submergence depth $S_d/D = 2.0$ is subjected to several incident wave heights of $H = 16$ and 31 mm with various wave frequencies ranged from 0.8 to 1.6 Hz. The cylinder is tuned to a frequency of 1.1 Hz based on the linear theory as follows. For a given wave frequency, $\omega/2\pi$, the power absorption efficiency is maximized by choosing the spring and damper constants as [8]:

$$k_{s,i} = (M_s + a_{ii})\omega^2 \ \text{ and } \ c_i = b_{ii} \quad (i = x, y) \tag{28}$$

where a_{ii} is the added mass representing the apparent increase of the cylinder inertia due to the liquid, and b_{ii} is the damping coefficient of the cylinder due to its forced oscillation in the ith direction. The non-dimensional added mass, $a_{ii}/\rho\forall$, and the dimensionless damping coefficient, $b_{ii}/\rho\omega\forall$, as a function of the non-dimensional submergence depth, S_d/R, and the dimensionless wave number, kR can be found in the literature [26,27].

In order to simulate each case, the dimensions of the computational domain must be adjusted according to the discussion given in Section 2.1. These dimensions according to Fig. 1 for a typical case, which is selected to be the conditions at the frequency of $f = 1.4$ Hz are: $Lc = 8.0$ m, $Hc = 0.5$ m, $d = 0.35$ m, $Ld1 = 0.25$ m, $Ld2 = 1.0$ m, $Xp = 0.5$ m, $Ls = 4.0$ m and $S_d = 0.1$ m. The values of the spring and damper constants in each direction are determined based on the linear theory for $f = 1.1$ Hz as $k_{sx} = k_{sy} = 826$ N/m and $c_x = c_y = 20$ Ns/m. A uniform mesh corresponding to 20 CPR is used in the entire computational domain. Also a time step equal to $T/100$ (where T is the

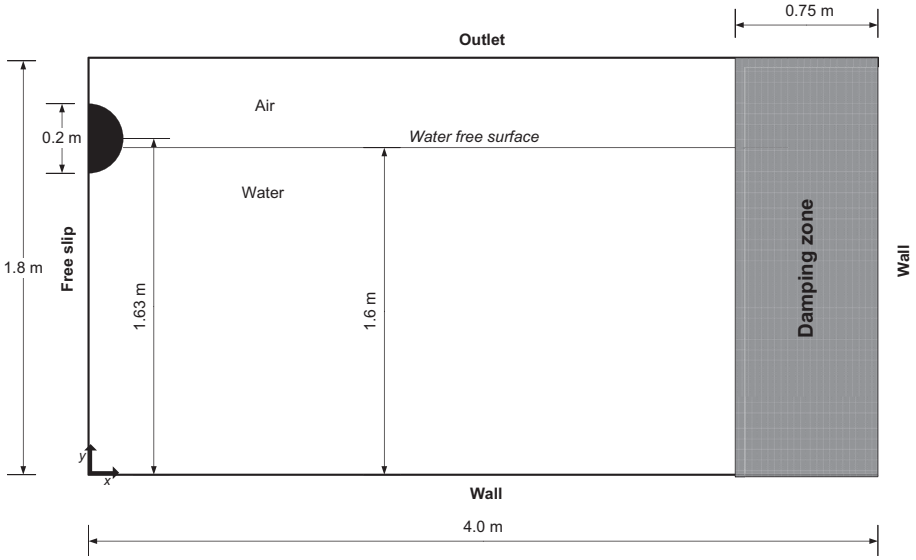

Fig. 6. The dimensions of the computational domain and the boundary conditions for the free decay of a circular cylinder on the free surface of a still water (the drawing is not to scale).

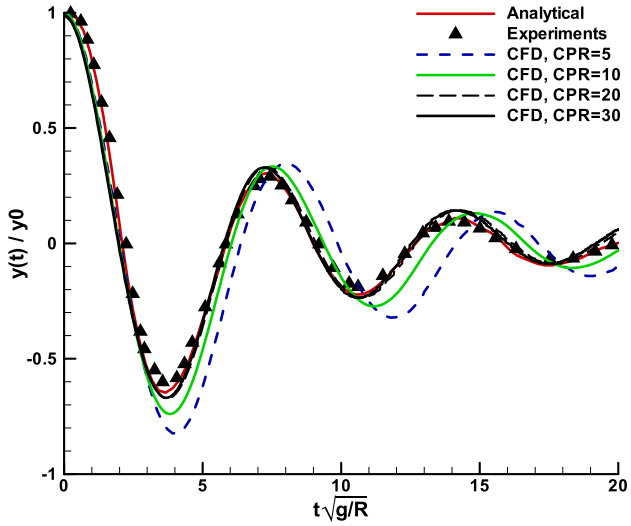

Fig. 7. The cylinder center position as a function of the non-dimensional time for the free decay of a circular cylinder on the free surface of a still water (Fig. 6).

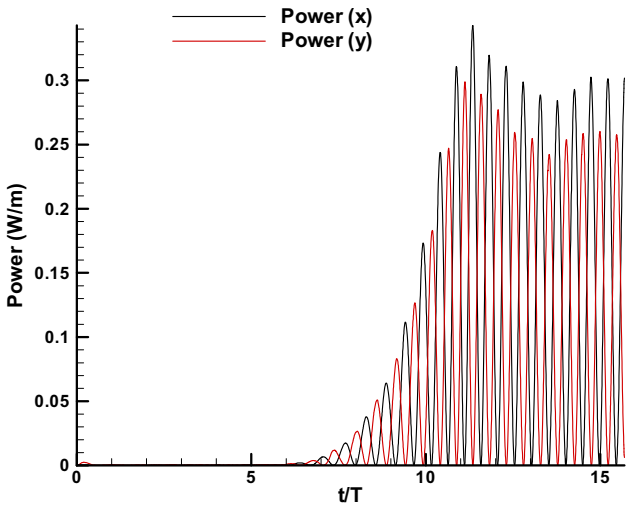

Fig. 9. Time variations of the absorbed power in the x and y directions, for $H = 31$ mm and $f = 1.4$ Hz corresponding to the circular cylinder WEC (Fig. 8).

wave period) is found to be sufficiently small such that the results were independent of the time step. The calculation time for this case is about 48 h on a single core 2.4 GHz PC computer.

The time evolution of the free surface profile as the flap starts its motion inside the water is shown in Fig. 8. The solid objects, which are the flap-type wavemaker and the submerged circular cylinder, are displayed in black. The wavemaker is forced to move with a prescribed simple harmonic motion in order to generate a 31 mm-height wave. The motion of the flapper is initiated using a linear timeramp with a duration of $2T$ to eliminate the initial instabilities [14]. The wave-generated motion of the submerged cylinder, however, is calculated based on the momentum conservation equations of the solid as described in Section 2.3.

The resultant absorbed power in the x and y-directions as a function of the non-dimensional time is shown in Fig. 9. After nearly 13 wave periods (including the initial time ramp) steady-state conditions are achieved. As the figure shows, the absorbed power in the x-direction is slightly greater than that of the y-direction. The total absorbed power is the sum of the power in the two orthogonal directions. The simulation is repeated for several wave frequencies for two wave heights of 16 and 31 mm with the values of the spring and damper constants tuned for $f = 1.1$ Hz. For these simulations, the incident wave characteristics including the wave number, wave steepness, wave group-velocity and wave power per meter of the crest are given in Table 1 for the 16-mm waves

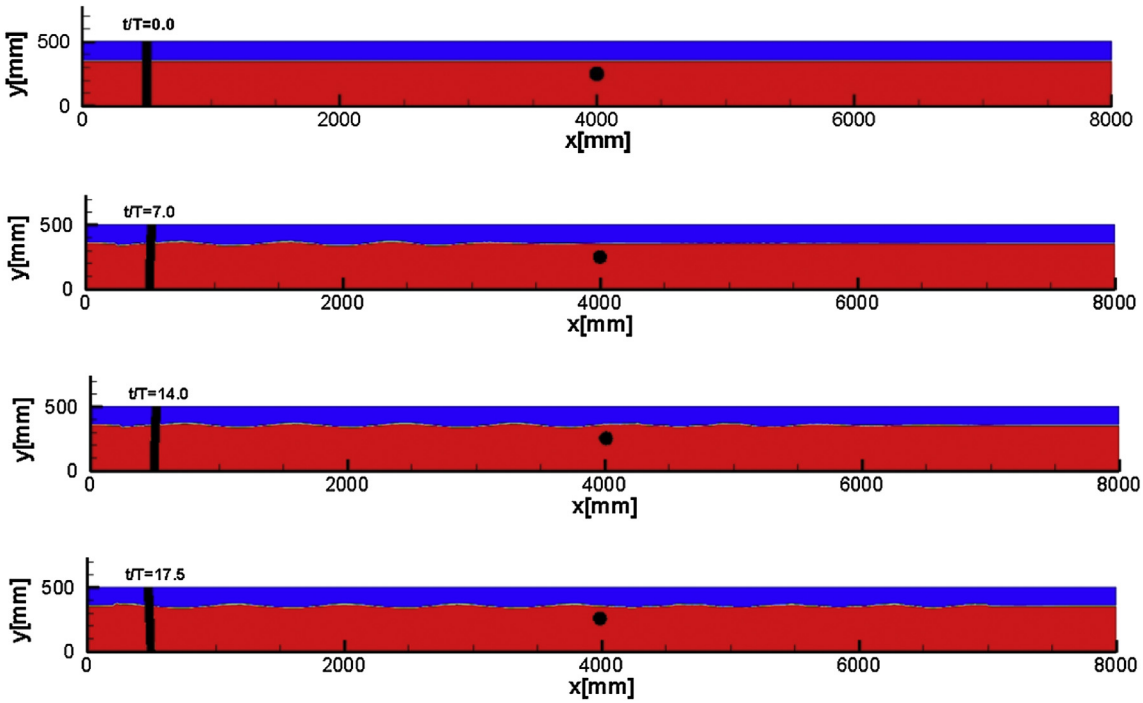

Fig. 8. Time evolution of the free surface profile for the interactions of the 31 mm incident waves at $f = 1.4$ Hz with the circular cylinder WEC (Fig. 1).

Table 1
Wave characteristics at various frequencies for the 16 mm-height waves.

Wave frequency (Hz)	Wave number k	kd	kR	$H = 16$ mm						
				H/L	c_g (m/s)	p_L (W/m)	$Re_x \times 10^{-3}$	KC_x	$Re_y \times 10^{-3}$	KC_y
0.8	3.19	1.12	0.160	0.008	1.168	0.367	3.928	0.492	2.604	0.326
0.9	3.76	1.32	0.188	0.010	1.036	0.325	3.847	0.428	2.830	0.315
1.0	4.41	1.54	0.221	0.011	0.913	0.287	3.756	0.376	3.009	0.301
1.1	5.15	1.80	0.258	0.013	0.803	0.252	3.653	0.333	3.131	0.285
1.2	5.98	2.09	0.299	0.015	0.710	0.223	3.535	0.295	3.191	0.266
1.3	6.93	2.43	0.347	0.018	0.635	0.199	3.399	0.262	3.186	0.246
1.4	7.97	2.79	0.399	0.020	0.576	0.181	3.245	0.232	3.121	0.223
1.5	9.09	3.18	0.455	0.023	0.529	0.166	3.071	0.205	3.002	0.201
1.6	10.33	3.62	0.517	0.026	0.492	0.154	2.879	0.180	2.843	0.178

Table 2
Wave characteristics at various frequencies for the 31 mm-heightwaves.

Wave frequency (Hz)	Wave number k	kd	kR	$H = 31$ mm						
				H/L	c_g (m/s)	p_L (W/m)	$Re_x \times 10^{-3}$	KC_x	$Re_y \times 10^{-3}$	KC_y
0.8	3.19	1.12	0.160	0.016	1.376	1.376	7.610	0.953	5.045	0.632
0.9	3.76	1.32	0.188	0.019	1.036	1.220	7.454	0.830	5.482	0.610
1.0	4.41	1.54	0.221	0.022	0.913	1.076	7.278	0.729	5.829	0.584
1.1	5.15	1.80	0.258	0.025	0.803	0.946	7.078	0.644	6.067	0.553
1.2	5.98	2.09	0.299	0.030	0.710	0.836	6.849	0.572	6.183	0.516
1.3	6.93	2.43	0.347	0.034	0.635	0.748	6.587	0.508	6.173	0.476
1.4	7.97	2.79	0.399	0.039	0.575	0.678	6.287	0.450	6.046	0.433
1.5	9.09	3.18	0.455	0.045	0.529	0.624	5.950	0.397	5.817	0.389
1.6	10.33	3.62	0.517	0.051	0.492	0.580	5.578	0.349	5.508	0.345

and in Table 2 for the 31-mm waves. Nearly all these cases fall within the range of the intermediate water depth ($\pi/10 \leq kd \leq \pi$). The oscillatory flow regime around structures can be characterized by two dimensionless numbers, the Reynolds (Re) and the Keulegan–Carpenter (KC) numbers, defined as:

$$\mathrm{Re} = \frac{\rho U_m D}{\mu} \tag{29}$$

$$\mathrm{KC} = \frac{U_m T}{D} \tag{30}$$

where U_m is the maximum flow velocity in a wave period T at the level of the cylinder center. The values of the Re and KC numbers for the x and y directions are also given in Tables 1 and 2. For the entire cases, the Reynolds number was less than 1×10^4 and the KC less than 1.0. Based on the experimental studies of Sarpkaya [28] and Honji [29], summarized by Sumer and Fredsoe [30], these conditions guarantees that the flow regime remains laminar.

Fig. 10 shows a comparison of the total energy absorption calculated in the present study with the numerical and experimental results of Davis [9] and also those of the linear theory [8]. As the figure shows, there is a substantial discrepancy between the experimental results and the predictions of the linear theory. The efficiency obtained from the measurements is considerably lower than that of the linear theory. The experimental data also shows that the maximum efficiency shifts toward higher frequencies as the wave height increases. The shift in the maximum efficiency implies that the values of the spring and damper constants are mistuned [9]. In other words, application of Eq. (28) in tuning the absorber for steep waves is questionable since this equation is obtained based on the linear theory assumptions. As seen in Fig. 10, although the numerical results of Davis [9] predict an efficiency drop to some extent, there is still a considerable discrepancy between these results and those of the measurements. In addition, the calculations of Davis [9] in contrast to his experiments predict the maximum efficiency to occur at the tuned frequency of 1.1 Hz.

From Fig. 10 it can be seen that the predictions from the developed model in the present study are in a better agreement with the experimental data in terms of both the efficiency values and the frequency of the maximum efficiency. Although the results of the present numerical model are in a convincing agreement with those of the experiments, still some discrepancy can be observed in Fig. 10. This might be attributed to the way the spring and damper constants are adjusted in the experiments. These values have been set up based on the maximum orbit diameter of the cylinder in the experiments of Davis [9] which may not necessarily represent the exact values calculated from the linear theory and used in the simulations.

The above observation regarding the shift of the maximum efficiency may be further explained by the fact that at the tuned frequency, a resonance should occur and the orbital motion of the

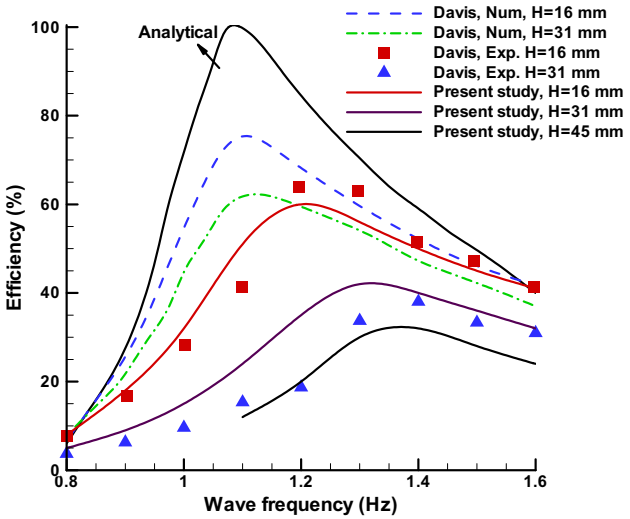

Fig. 10. Wave absorption efficiency in comparison with the experimental and numerical results of Davis [9] and those of the analytics [8].

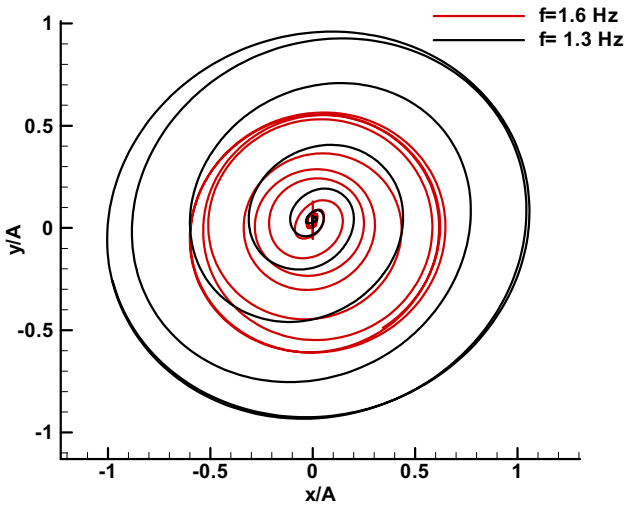

Fig. 11. Cylinder center position exposed to 31 mm waves with $f = 1.3$ and 1.6 Hz, ($A = 0.0155$ m).

cylinder should increase considerably. The added mass and the damping coefficient used to tune the cylinder are obtained for small oscillatory motions of a cylinder in an inviscid fluid. These conditions are violated especially around the resonance conditions where the cylinder experiences large displacements. Fig. 11 shows the transient non-dimensional center position of the solid cylinder obtained from simulations for the 31-mm waves at the frequency of the maximum efficiency point ($f = 1.3$ Hz) in comparison with that of the highest considered frequency ($f = 1.6$ Hz). As can be observed, the range of the movement of the cylinder center at the maximum efficiency is nearly two times larger than that of the 1.6 Hz. This might be a reason for the fact that the maximum efficiency points in the experiments do not coincide with the tuned frequencies calculated based on the linear theory.

4.4. Steeper waves

The largest wave heights in the experiments of Davis [9] are 31-mm waves in a water depth of $d = 0.35$ m. The maximum wave steepness in his experiments is $H/L = 0.051$ which occurs at the maximum frequency of the tests ($f = 1.6$ Hz). In practice, however, a submerged cylinder WEC might be exposed to steeper waves at various water depths. The numerical wave tank developed in the current study is capable of reproducing the fully nonlinear interactions of viscous water waves with two-dimensional bodies as long as the turbulence phenomena are not important. Assuming the flow to be laminar, the method is applied to highly steep waves, $H/L = 0.074$, but still far enough from breaking. Similar conditions to the experiments of Davis [9] (discussed in the previous section) are considered, but with wave heights of 45 mm. The incident wave characteristics including the corresponding Re and KC numbers are given in Table 3. For these cases, the laminar flow assumption is valid for the wave frequencies in the range of 1.1–1.6 Hz [30].

The water free surface profiles for the case with a maximum wave steepness ($H/L = 0.074$ at $f = 1.6$ Hz) at various non-dimensional times are shown in Fig. 12. For this case a time ramp equal to $4T$ is used for the initiation of the flap-type wavemaker motion. As the figure shows, after nearly 12 wave periods the first significant wave height reaches the cylinder. Clearly, the resultant wave-generated motion of the cylinder increases as the wave height increases. The center position of the cylinder when subjected to the 45-mm wave is compared with the one subjected to 31-mm wave in Fig. 13 at the wave frequency of $f = 1.6$ Hz. They are both non-dimensionalized using the amplitude of the 31-mm wave ($A = 0.0155$ m). For the wave with a higher height, a considerable increase in the orbital motion of the cylinder is evident. This, of course will lead to a more departure from the validity of the linear theory assumptions used in tuning the cylinder. As a result, a more reduction in the absorption efficiency is expected. The calculated total power absorbed for the 45-mm waves is also shown in Fig. 10. As can be seen, the efficiency for the 45-mm waves is dropped compared to those of the 31 and 16-mm waves; also, the maximum efficiency point has further moved toward higher frequencies. As the results indicate, the submerged cylinder WEC has a self-limiting quality. In other words, although the input wave power increases as height square, the fall in efficiency counteracts this positive effect by limiting the power absorbed.

4.5. Tuning at large wave heights

As stated in the previous sections, the mistuning of the WEC is a reason for the efficiency drop as the wave height increases. Accordingly, in this section the effects of the spring and damper constants on the absorption efficiency are investigated separately for conditions similar to those considered by Davis [9] in his experiments discussed in previous sections. Fig. 14 shows the effect of the damping coefficient on the absorption efficiency at $f = 1.1$ Hz for three different wave heights while the spring constant was held fixed at its value calculated based on the linear theory. The damping coefficients are non-dimensionalized using the value calculated based on the linear theory (named here c_L). Clearly, at $c/c_L = 0.0$ no energy is absorbed. As the figure shows, for all the wave heights the maximum efficiency point occurs in a damping coefficient larger than that of the linear theory. However, the maximum efficiency point moves toward higher non-dimensional damping coefficients as the wave height increases. Such a behavior suggests that providing a mechanism which enables controlling the damping coefficient might be very helpful in increasing the energy absorption efficiency of the WEC when

Table 3
Wave characteristics at various frequencies for the 45-mm height waves.

Wave frequency (Hz)	Wave number k	kd	kR	$H = 45$ mm						
				H/L	c_g (m/s)	p_L (W/m)	$Re_x \times 10^{-3}$	KC_x	$Re_y \times 10^{-3}$	KC_y
0.8	3.19	1.12	0.160	0.023	1.168	2.900	11.047	1.384	7.324	0.917
0.9	3.76	1.32	0.188	0.027	1.036	2.573	10.821	1.205	7.958	0.886
1.0	4.41	1.54	0.221	0.032	0.913	2.267	10.565	1.059	8.462	0.848
1.1	5.15	1.80	0.258	0.037	0.803	1.994	10.274	0.936	8.807	0.802
1.2	5.98	2.09	0.299	0.043	0.710	1.763	9.942	0.830	8.976	0.749
1.3	6.93	2.43	0.347	0.050	0.635	1.577	9.561	0.737	8.961	0.691
1.4	7.97	2.79	0.399	0.057	0.576	1.430	9.126	0.653	8.776	0.628
1.5	9.09	3.18	0.455	0.065	0.529	1.314	8.637	0.577	8.444	0.564
1.6	10.33	3.62	0.517	0.074	0.492	1.221	8.097	0.507	7.996	0.501

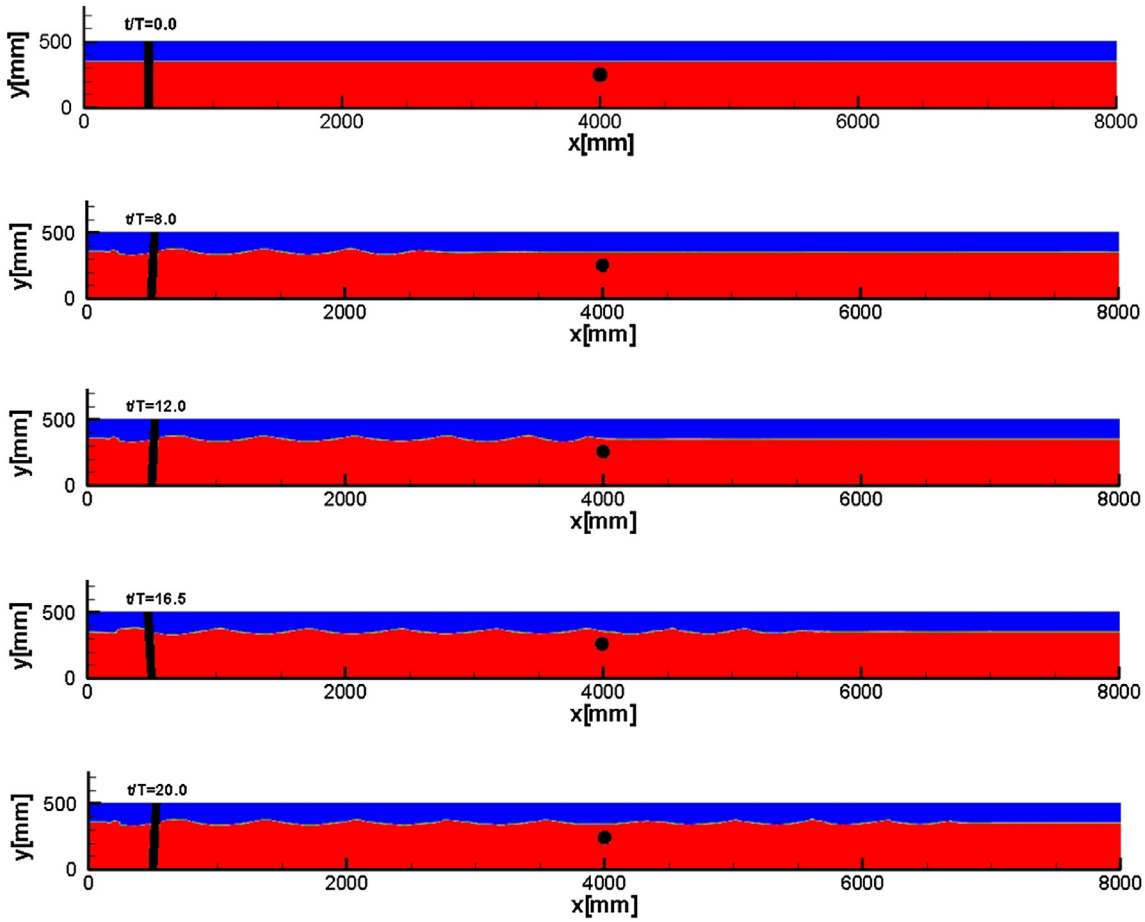

Fig. 12. Time evolution of the free surface profile for the 45 mm incident waves at $f = 1.6$ Hz interacting with the circular cylinder WEC (Fig. 1).

subjected to large incident waves. Similarly, in Fig. 15 the effect of spring constant on the absorption efficiency is shown when the damping coefficient was held fixed at its value calculated based on the linear theory (named here k_{sL}) for $f = 1.1$ Hz. Unlike the damping coefficient, the maximum efficiency point moves toward lower non-dimensional spring constants as the wave height increases. Compared to Fig. 14, the values of the non-dimensional spring constants at the maximum efficiency points are closer to the values determined based on the linear theory. In other words, the results of the absorption efficiency are more sensitive to the values of the spring constant in comparison with those of the damping coefficient.

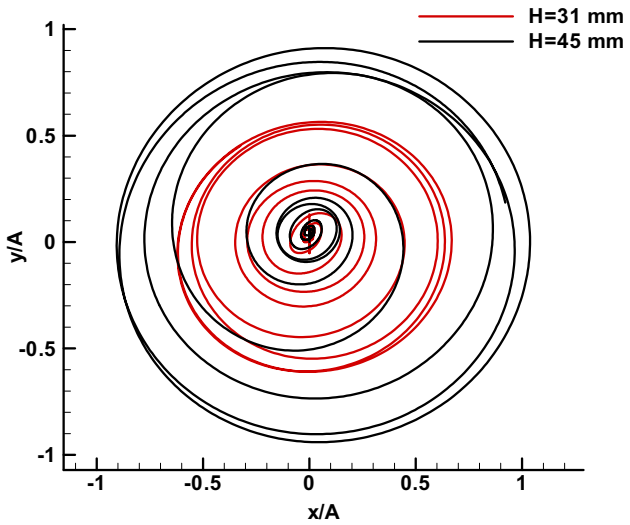

Fig. 13. Cylinder center position at $f = 1.6$ Hz for two wave heights, $H = 31$ and 45 mm, both non-dimensionalized using the 31-mm wave amplitude ($A = 0.0155$ m).

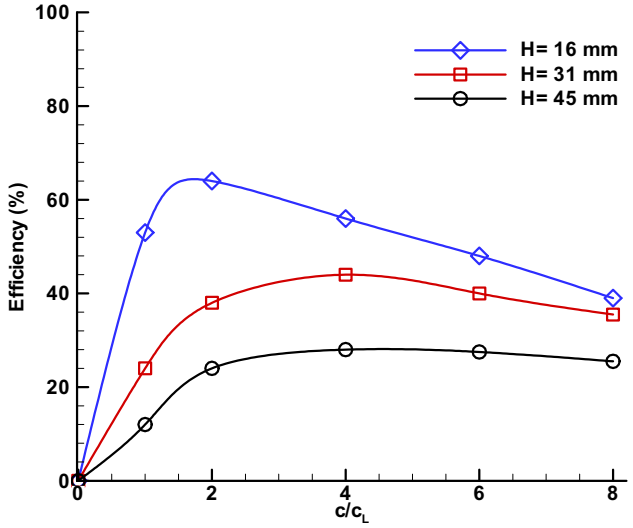

Fig. 14. Efficiency variations at various dimensionless damping coefficients at $f = 1.1$ Hz, $d = 0.35$ m, $S_d = 0.1$ m, $S_d/R = 2.0$, $k_s = 826$ N/m.

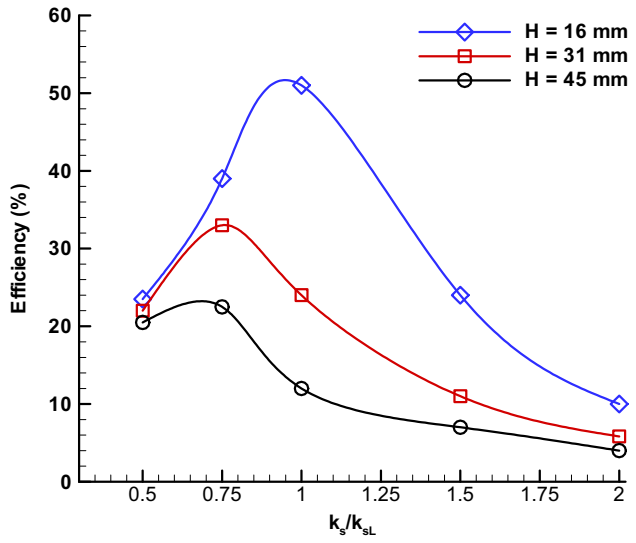

Fig. 15. Efficiency variations at various dimensionless spring constants at $f = 1.1$ Hz, $d = 0.35$ m, $S_d = 0.1$ m, $S_d/R = 2.0$, $c = 20$ N/m.

5. Conclusions

A numerical model based on the complete solution of the Navier–Stokes equations is proposed in order to investigate the behavior of the submerged cylinder wave energy converter (WEC). The solution is obtained using a control volume approach in conjunction with the fast-fictitious-domain-method for treating the solid objects. In the numerical wave tank developed in this study, both the prescribed harmonic motion of the flap-type wavemaker and the wave-generated motion of the submerged cylinder WEC are simulated. For validating the model, the free vibrations of a solid object in various non-dimensional damping ratios and the free decay of a heaving circular cylinder on the free surface of a still water are simulated. The numerical results are compared with those of the analytics where a good agreement is observed. Next, the wave energy absorption efficiency of a circular cylinder WEC calculated from the model is compared with that of the available experiments in similar conditions. The results of numerical simulations for steep waves show that the wave energy absorption of the cylinder falls off substantially as the wave height increases. Moreover, the maximum efficiency point moves toward higher wave frequencies with increasing the wave height. In other words, tuning the cylinder based on the linear theory does not work well for steep waves. Therefore, the effects of the spring and damping constants on the absorption efficiency are investigated using the developed numerical wave tank. Results show that as the wave height increases, the maximum efficiency of the submerged cylinder WEC occurs in larger damping coefficients relative to those calculated based on the linear theory. Conversely, the maximum efficiency as the wave height increases moves toward lower spring constants relative to those of the linear theory. As long as the turbulence phenomena are not important, the proposed numerical wave tank can be effectively incorporated in the design of the submerged cylinder WEC for a wide range of Reynolds and Keulegan–Carpenter numbers.

Nomenclature

A	wave amplitude
c	damping coefficient
c_x, c_y	damping coefficients in x and y directions, respectively
d	still water depth
$\vec{F}_b$	body forces
f	wave frequency
F	liquid volume fraction
g	gravitational acceleration
H	wave height $= 2A$
Hc	height of the computational domain
k	wave number
k_{sx}, k_{sy}	spring constants in x and y directions, respectively
L	wave length
Lc	length of the computational domain
$Ld1$, $Ld2$	length of the damping zones
Ls	position of the submerged cylinder
p	pressure
R	cylinder radius
S_d	submergence depth
t	time
u_s	horizontal velocity of the solid object
$\vec{V}$	velocity vector
v_s	vertical velocity of the solid object
$\forall$	volume
x	horizontal coordinate distance
$x_{c,\,s}$	the center position of the solid object in the x-direction
x_{free}	spring free length in the x direction
y	vertical coordinate distance
$y_{c,\,s}$	the center position of the solid object in the y-direction
y_{free}	spring free length in the y direction
μ	dynamic viscosity
ρ	density
τ	stress tensor
φ_s	solid volume fraction
ω	angular frequency
η	free surface elevation

References

[1] McCormick ME. Ocean wave energy conversion. New York: Wiley; 1981.
[2] Falcão AFdO. Wave energy utilization: a review of the technologies. Renew Sust Energy Rev 2010;14:899–918.
[3] Evans DV. A theory for wave-power absorption by oscillating bodies. J Fluid Mech 1976;77:1–25.
[4] Dean WR. On the reflection of surface waves by a submerged circular cylinder. Proc Camb Philos Soc 1948;44:483–91.
[5] Ogilvie TF. First- and second-order forces on a cylinder submerged under a free surface. J Fluid Mech 1963;16:451–72.
[6] Heikkinen H, Lampinen MJ, Böling J. Analytical study of the interaction between waves and cylindrical wave energy converters oscillating in two modes. Renew Energy 2013;50:150–60.
[7] Payne GS, Taylor JRM, Bruce T, Parkin P. Assessment of boundary-element method for modelling a free-floating sloped wave energy device. Part 2: Experimental validation. Ocean Eng 2008;35:342–57.
[8] Evans DV, Jeffrey DC, Salter SH, Taylor JRM. Submerged cylinder wave energy device: theory and experiment. Appl Ocean Res 1979;1:3–12.
[9] Davis JP. Wave energy absorption by the Bristol cylinder-linear and non-linear effects. Proc Inst Civil Eng 1990;89:317–40. Part 2.
[10] Morison JR, O'Brien MP, Johnson JW, Schaaf SA. The force exerted by surface waves on piles. J Petrol Technol 1950;2:149–54.
[11] Babarit A, Hals J, Muliawan MJ, Kurniawan A, Moan T, Krokstad J. Numerical benchmarking study of a selection of wave energy converters. Renew Energy 2012;41:44–63.
[12] Sharma N, Patankar NA. A fast computation technique for the direct numerical simulation of rigid particulate flows. J Comput Phys 2005;205:439–57.
[13] Mirzaii I, Passandideh-Fard M. Modeling free surface flows in presence of an arbitrary moving object. Int J Multiphase Flow 2012;39:216–26.
[14] Anbarsooz M, Passandideh-Fard M, Moghiman M. Fully nonlinear viscous wave generation in numerical wave tanks. Ocean Eng 2013;59:73–85.
[15] Glowinski R, Pan TW, Hesla TI, Joseph DD. A distributed Lagrange multiplier/fictitious domain method for particulate flows. Int J Multiphase Flow 1999;25:755–94.
[16] Glowinski R, Pan TW, Hesla TI, Joseph DD, Périaux J. A fictitious domain approach to the direct numerical simulation of incompressible viscous flow past moving rigid bodies: application to particulate flow. J Comput Phys 2001;169:363–426.

[17] Patankar NA. A formulation for fast computations of rigid particulate flows. In: Center for Turbulence Research, editor. Annual research briefs. Evanston: Northwestern University; 2001. pp. 185–96.
[18] Patankar NA, Singh P, Joseph DD, Glowinski R, Pan TW. A new formulation of the distributed Lagrange multiplier/fictitious domain method for particulate flows. Int J Multiphase Flow 2000;26:1509–24.
[19] Harlow FH, Amsden AA. Fluid dynamics: a LASL monograph (mathematical solutions for problems in fluid dynamics). Los Alamos Scientific Laboratory report LA 4700; 1971.
[20] Kershaw DS. The incomplete Cholesky-conjugate gradient method for the iterative solution of systems of linear equations. J Comput Phys 1978;26:43–65.
[21] Youngs DL. An interface tracking method for a 3D Eulerian hydrodynamics code; 1984.
[22] Rao SS. Mechanical vibrations. 5th ed. Prentice Hall; 2004.
[23] Ursell F. The decay of the free motion of a floating body. J Fluid Mech 1964;19:305–19.
[24] Maskell SJ, Ursell F. The transient motion of a floating body. J Fluid Mech 1970;44:303–13.
[25] Ito S. Study of the transient heave oscillation of a floating cylinder. Department of Ocean Engineering, Massachusetts Institute of Technology; 1977.
[26] Greenhow M, Ahn SI. Added mass and damping of horizontal circular cylinder sections. Ocean Eng 1988;15:495–504.
[27] Evans DV, Porter R. Wave-free motions of isolated bodies and the existence of motion-trapped modes. J Fluid Mech 2007;584:225–34.
[28] Sarpkaya T. Force on a circular cylinder in viscous oscillatory flow at low Keulegan—Carpenter numbers. J Fluid Mech 1986;165:61–71.
[29] Honji H. Streaked flow around an oscillating circular cylinder. J Fluid Mech 1981;107:509–20.
[30] Sumer BM, Fredsoe J. Hydrodynamics around cylindrical structuresIn Advanced series on Ocean Engineering, vol. 12. World Scientific; 1997.